Chapter 9
Automatic Atlas-Free Multiorgan Segmentation of Contrast-Enhanced CT Scans

Assaf B. Spanier and Leo Joskowicz

Abstract Automatic segmentation of anatomical structures in CT scans is an essential step in the analysis of radiological patient data and is a prerequisite for large-scale content-based image retrieval (CBIR). Many existing segmentation methods are tailored to a single structure and/or require an atlas, which entails multistructure deformable registration and is time-consuming. We present a fully automatic atlas-free segmentation of multiple organs of the ventral cavity in contrast-enhanced CT scans of the whole trunk (CECT). Our method uses a pipeline approach based on the rules that determine the order in which the organs are isolated and how they are segmented. Each organ is individually segmented with a generic four-step procedure. Our method is unique in that it does not require any predefined atlas or a costly registration step and in that it uses the same generic segmentation approach for all organs. Experimental results on the segmentation of seven organs—liver, left and right kidneys, left and right lungs, trachea, and spleen—on 20 CECT scans of the VISCERAL Anatomy training dataset and 10 CECT scans of the test dataset yield an average DICE volume overlap similarity score of 90.95 and 88.50%, respectively.

Source code is available at:
http://www.cs.huji.ac.il/~caslab
https://bitbucket.org/shpanier/cbir_anatomy3

A.B. Spanier (✉) · L. Joskowicz
The Rachel and Selim Benin School of Computer Science and Engineering,
The Hebrew University of Jerusalem, Jerusalem, Israel
e-mail: assaf.spanier@mail.huji.ac.il

L. Joskowicz
e-mail: leo.josko@mail.huji.ac.il

A. Hanbury et al. (eds.), *Cloud-Based Benchmarking of Medical Image Analysis*, DOI 10.1007/978-3-319-49644-3_9

9.1 Introduction

Volumetric medical images, including computed tomography (CT) and magnetic resonance imaging (MRI) are pervasive in routine clinical practice. Worldwide, the number of these images reaches into the hundreds of millions per year and is growing at a fast pace [19]. Radiologists and physicians rely upon these images for diagnosis, treatment strategy and follow-up evaluation. Currently, these medical images and the patient records associated with them are used primarily for diagnosis and follow-up of the primary condition without further analysis between and across the patients. The vast amount of information in these valuable clinical datasets represents an untapped gold mine that could support a wide variety of clinical tasks, such as the retrieval of patient cases with similar radiology images, image-based retrospective incidental findings, large-scale radiological population and epidemiological studies, and preventive medicine by early radiological detection. Indeed, the application of big data analytics to the field of medical imaging has been largely absent despite the fact that clinical imaging represents the largest single component of the medical health record.

Radiology content-based image retrieval (CBIR) is a key enabler for the utilization of previously acquired imaging data to assist radiologists in the decision-making process [11, 24, 31]. A CBIR system is an image search engine that retrieves medical records of patients with similar images from large archives. CBIR systems rely on the automatic extraction of imaging features from a non-annotated medical images database. The features include specific properties of anatomical structures, such as organ volume, shape and texture, which are automatically computed from the image and are used to compare images.

Today, most of the CBIR systems are based on global feature extraction [4]. Global features are extracted from the images with no prior knowledge regarding the content of the image, the organs and/or the pathologies and their location in the image. However, there is a discrepancy between the low-level features that are automatically extracted by the computer and the high-level concepts of human vision and image understanding: this gap is known as the semantic gap [8]. The isolation and delineation of individual structures in the images—referred to as segmentation—provides a strong shape and location prior that is expected to improve the quality of the automatic feature extraction process, thereby significantly improving the performance of CBIR systems [25, 27].

The automatic segmentation of anatomical structures in volumetric medical images is widely recognized as a difficult and time-consuming task. Anatomical structures are numerous and complex: each has unique, distinctive characteristics and shows extensive biological variability across the patients [22]. In volumetric images, many structures have similar radiological tissue properties—attenuation coefficients in CT and relaxation times in MRI—which result in very low or no contrast between adjacent structures. Volumetric images also show great variability due to a plethora of CT/MRI scanners and scanning protocols, which produce scans with very different image properties, e.g. resolution, contrast and noise.

Numerous segmentation algorithms have been developed in the past three decades. These include region growing, ray casting [16], energy active contours [3], graph cut [2], level sets [30], statistical shape model [10], rule-based methods [26] and hybrid methods [5, 9]. Additionally, a large variety of methods for segmentation of nearly all anatomical structures, organs and pathologies in CT scans have been proposed. Examples of reviews of the existing approaches for some of the main organs include Mharib et al. [18] for liver segmentation, Sluimer et al. [28] for lungs segmentation and Freiman et al. [6] for kidney segmentation.

Most of the segmentation algorithms require prior models in the form of parameter values, intensity thresholds, shape priors, atlases and a database of previous cases. Some rely on user inputs such as seeds, regions of interest and/or initial delineations to produce the segmentation. In addition, most of the segmentation algorithms are optimized for a single structure and require significant effort to transfer/adapt to new structures. Also, single structure segmentation methods usually do not take into account the contextual information of the adjacent structures which may be exploited for the identification task.

Multistructure segmentation methods have been recently proposed to exploit this contextual information [23]. They usually require an atlas of the structures of interest, which consists of parametric shape models of the structures and their relative location in the body. This approach is currently the state of the art in brain structure segmentation [1]. More recently, atlas-based methods have been developed for organ segmentation of body CT scans [29, 33]. These methods require the construction of atlases, which usually relies on the manual segmentation of the structures of interest in the CT/MRI scans and their alignment to a reference scan. To obtain a segmentation of the structures of interest in a new scan, the atlas is matched to the scan and the structure models using deformable registration techniques [21]. The drawbacks of this approach are that the atlas construction is laborious, biased to the cases that are used to construct it and thus may suffer from low specificity (the generality of such a model may hamper the segmentation of a specific target image due to the large intersubject variability in the learning cases). In addition, multiatlas-based methods require deformable registration and incur a high computational cost.

To summarize, although many segmentation algorithms have been developed, they are unlikely to be useful for radiology CBIR either due to their focus on a single organ, their need for a predefined atlas, their lack of robustness and/or their prohibitive computational cost.

In this paper, we present a robust multiorgan fully automatic atlas-free segmentation method for the organs of the ventral cavity in contrast-enhanced CT scans of the whole trunk (CECT). Our method is specifically designed for radiology CBIR. It uses a pipeline approach based on the rules that determine the order in which the organs are isolated and how they are segmented. Each organ is individually segmented with a generic four-step procedure. Our method is unique in that it does not require any predefined atlas or registration and in that it uses the same generic segmentation approach for all organs.

Fig. 9.1 The CECT field of view starts at about the corpus mandibulae (i.e. in between the skull base and the neck) and ends at the pelvis. The scan is enhanced by an iodine-containing contrast agent commonly administered to improve tissue contrast, in order to detect pathological lymph nodes or organ affection of the lymphoma

We evaluate our method using the VISCERAL [17] publicly available database and make our source code openly available for the benefit of the community.[1] Experimental results on the 20 CECT scans of the VISCERAL Benchmark training dataset and 10 CECT scans of the test dataset yield an average DICE volume overlap similarity score of 90.95 and 88.50%, respectively.

9.2 Method

We describe next a new robust, multiorgan, fully automatic, atlas-free segmentation method of the organs of the ventral cavity in CECT scans. The input is CECT scans of the whole trunk (Fig. 9.1), with the patient properly positioned on their back. The field of view starts between the skull base and the neck and ends at the pelvis, and with none of the seven organs to be segmented missing. The output of our method is a segmentation of the seven organs of the ventral cavity: the trachea, both lungs, both kidneys, the spleen and the liver. Our method consists of two processes: the first is a scan-specific characterization process that determines the grey values of the high blood content organs (i.e. kidneys, spleen, and liver), and a localization of six cross sections of interest in the scan. The second is a generic four-step pipeline

[1] http://www.cs.huji.ac.il/~caslab.

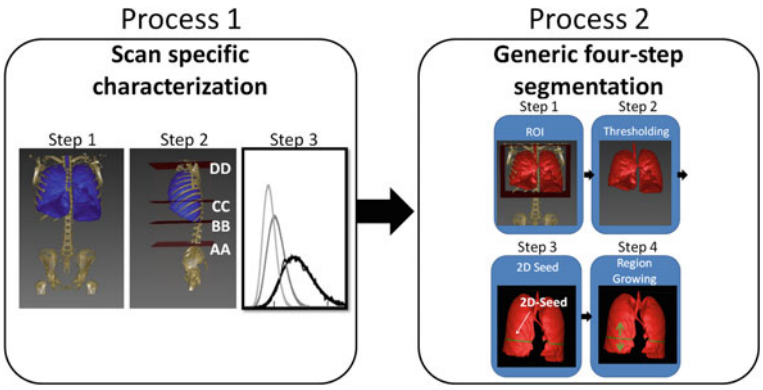

Fig. 9.2 Our method consists of two processes: (1) a scan-specific characterization process that locates six cross sections of interest in the scan along with the grey-level values of the high blood content organs (Process 1) and (2) a four-step pipeline segmentation process for segmenting each organ (Process 2)

segmentation process followed by a fine-tuning post-processing step. The method is illustrated in Fig. 9.2 and summarized in Table 9.1.

Next, we describe the two processes, followed by details of the implementation for seven ventral cavity organs: the trachea, the left and right lungs, the left and right kidneys, the spleen and the liver.

9.2.1 Process 1: Scan-Specific Characterization

The goal of the scan-specific characterization process is to locate six cross sections of interest in the CECT scan along with the grey-level values of the high blood content organs. There are three steps in this process: (1) isolation of the bone skeleton and the breathing system (lungs and trachea), (2) localization of six cross sections of interest inside the body and (3) identification of the grey-level values of the high blood content organs (i.e. kidneys, spleen and liver). Below is a detailed description of each step.

1. **Bone Skeleton and Breathing System Isolation**: We start by isolating the patient's body from the background (air and scan gantry) based on the location and intensity values. We then identify the bone skeleton and the breathing system (lungs and trachea). Next, we isolate the largest connected components that contain grey levels above 250 HU for the skeleton and the largest connected components that contain grey levels between −1000 and −500 HU for the breathing system.
2. **Cross-Sectional Localization**: We define six cross sections of interest, which will be used to define the ROI of the various organs, they are marked by labels

Table 9.1 Summary of the detailed implementation of the four-step segmentation for each organ. The rows in the table represent the steps of the segmentation algorithm, the seven columns list the parameters for each organ at each step. Abbreviations used in the table: *AA*—the narrowest slice of bones in the beginning of the lumbar region, *BB*—the inferior slice of the breathing system, *CC*—the widest slice of the breathing system, *DD*—the superior slice of the breathing system (the narrowest slice of the breathing system) and *FF* - the plane that bisects the spinal column at 45° (Fig. 9.3). μ_{BV} and σ_{BV} stand for the average and the standard deviation of the lungs' blood vessels' grey-level values. μ_{kmean} stands for the average of the two cluster centres produced by the k-means clustering algorithm—with $k = 2$—to cluster all voxels confined by slices *AA*, *CC* and to the left of *EE* and that have grey-level values between zero and $\mu_{BV} + 3\sigma_{BV}$

Steps			Trachea	Lungs	Left kidney	Spleen	Right kidney	Liver
ROI	Axial	Upper	*DD*	*DD*	*CC*	*CC*	*CC*	*CC*
		Lower	*BB*	*BB*	*AA*	*AA*	*AA*	*AA*
	Sagittal coronal		ALL	ALL	left side of *FF*	left side of *FF*	right side of *FF*	right side of *FF*
Threshold	Upper value		$-500HU$	$-500HU$	$\mu_{BV} + 3\sigma_{BV}$	μ_{kmean}	$\mu_{BV} + 3\sigma_{BV}$	μ_{kmean}
	Lower value		$-1000HU$	$-1000HU$	μ_{kmean}	$\mu_{BV} - 0.5\sigma_{BV}$	μ_{kmean}	$\mu_{BV} - 0.5\sigma_{BV}$
2D seed identification			*DD*	*CC*	Widest in the ROI	The first slice above the left kidney	Widest in the ROI	The first slice above the left kidney
Slice region growing			Upwards to the top of the ROI and downwards to the first bifurcation.	Spectral clustering to isolate each lung	Upwards and downwards in the ROI. Between each pair of slices, the regiongrowing continues only into the largest connected component			
Post-processing, control mechanism			Post-processing includes a number of morphological operators; segmentations below 30% of average organ volume are excluded					

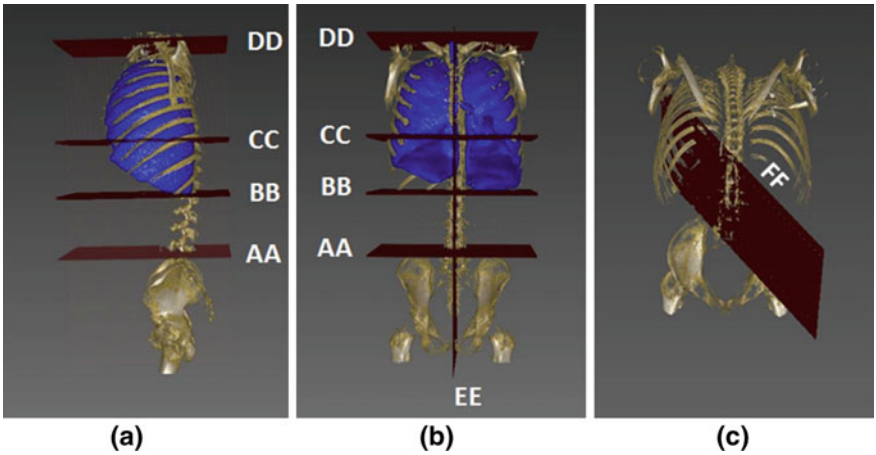

Fig. 9.3 Localization of six cross sections: *AA*—the narrowest slice of bones in the beginning of the lumbar region; *BB*—the inferior slice of the breathing system; *CC*—the widest slice of the breathing system; and *DD*—the superior slice of the breathing system (which is also the narrowest slice of the breathing system). *EE*—the sagittal symmetrical plane; *FF*—a plane bisecting the spinal column at 45°

AA through *FF* in Fig. 9.3. Four of the cross sections are axial, one is sagittal and one is diagonal. The cross sections are: (1) the narrowest slice of bones in the beginning of the lumbar region (marked by *AA*), hereinafter the narrowest slice and widest slice are defined by measuring the perimeter of the 2D convex hull in the axial slice; (2) the inferior slice of the breathing system (marked by *BB*); (3) the widest slice of the breathing system (marked by *CC*); (4) the superior slice of the breathing system, which is also the narrowest slice of the breathing system (marked by *DD*); (5) the sagittal plane through the middle of the spinal column (marked by *EE*); and (6) the plane that passes through the centre of the spinal column at 45° (marked by *FF*). Slice *AA* is found by starting at slice *BB* and moving inferiorly slice by slice along the axial planes, when the bone perimeter increases by over 200%, that slice is defined as *AA*. To define planes *EE* and *FF*, we construct a bounding box around the bone cross section at slice *BB*; *EE* is the sagittal symmetrical plane bisecting it; and *FF* is the plane bisecting it at 45°.

3. **Grey-Level-Value Identification**: We first identify the grey level of the lungs' blood vessels by isolating all voxels with values that are greater than zero inside the lungs (Fig. 9.4). We denote the average and the standard deviation of these blood vessels' grey-level values as μ_{BV} and σ_{BV}, respectively. Next, we apply the k-means clustering algorithm with $k = 2$ on all voxels confined by slices *AA*, *CC* and to the left of *EE* and that have grey-level values between zero and $\mu_{BV} + 3\sigma_{BV}$. We denote the average of those two cluster centres as μ_{kmean}. These values will be used to define the thresholds that differentiate between the kidneys, the spleen and the liver.

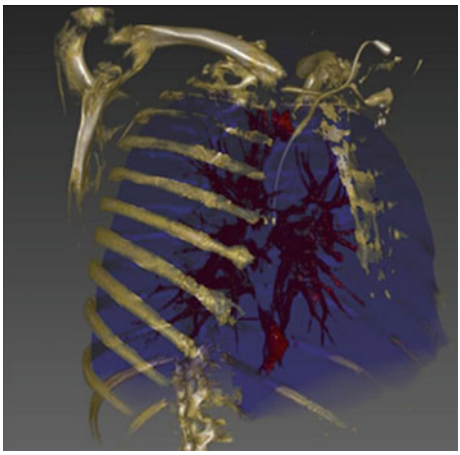

Fig. 9.4 Illustration of grey-level values estimation: Inside the breathing system (*blue*), all voxels that contain grey-level values greater than zero (*red*) are the lungs' blood supply. The grey-level values of other organs in the scan are estimated by computing the average and standard deviation of those voxels

9.2.2 Process 2: Generic Four-Step Segmentation

In the generic four-step segmentation process, organs are isolated and segmented, from the simplest one to the most difficult one. Using the cross sections and the grey-level values identified by the first process, the four-step framework is applied to the organs in the following order. First, the breathing system organs (i.e. the trachea and the lungs) are segmented. Next, the high blood content organs (i.e. kidneys, spleen, and liver) are segmented, first those on the left, which are better separated, then those on the right. For each organ, the process starts with a coarse segmentation that is refined along the further steps until the final segmentation is obtained. The organ segmentation order prevents the ambiguous assignment of the same image region to multiple organs, as previously segmented image regions are excluded from the later segmentation process. We describe next the four successive steps. In addition, Table 9.1 summarizes the details and parameters for this process.

1. ROI Identification—The region of interest (ROI) is extracted and constitutes a coarse initial segmentation. This step is organ-dependent and is based on the location of the organ in the ventral cavity in the current scan.
2. Thresholding—After ROI identification, we threshold the CECT scan to fine-tune the coarse segmentation of the organ based on its unique grey-level characteristics. Note that the thresholding value derived in Process 1 is organ specific and scan specific.
3. 2D Seed Identification—A representative 2D axial slice of the organ in the CECT scan is identified. This slice serves as the set of seeds for the region-growing step.
4. Slice Region Growing—Organ segmentation by 3D region growing starting from the 2D seed (2D axial slice) to obtain the final segmentation of the organ.

Figure 9.5 illustrates each of the four steps for the segmentation of the lungs.

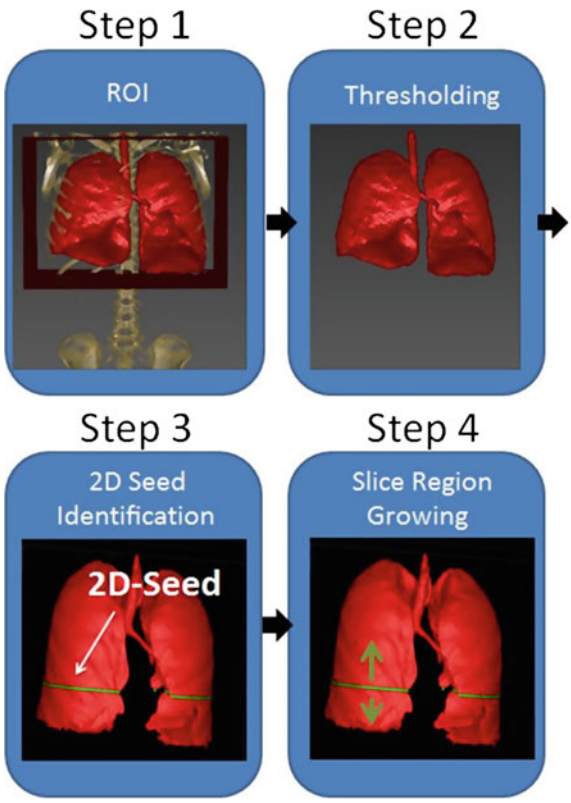

Fig. 9.5 Illustration of the four steps of Process 2 on the lungs: (1) The breathing system (lungs and trachea) ROI, (2) thresholding it with a scan-specific and structure-specific value, (3) 2D axial slice that serves as the set of seeds for region growing, (4) 3D region growing starting from the 2D seed upwards and downwards inside the ROI

9.2.3 Process 2: Implementation details

Below are the details of the implementation of the four-step segmentation process for seven ventral cavity organs: the trachea, the left and right lungs, the left and right kidneys, the spleen and the liver.

Step 1: ROI Identification

The ROI of each organ is obtained as follows:

Lungs and Trachea: The lungs and trachea are located within the region confined by slices *BB* and *DD*, as illustrated in Fig. 9.5, Step 1.

Left Kidney and Spleen: The left kidney and spleen are located within the region defined by slices *AA*, *CC* and the area to the left of *FF*, as illustrated in Fig. 9.6.

Right Kidney and Liver: The right kidney and the liver are located within the region defined by slices *AA*, *CC* and the area to the right of *FF* as illustrated in Figs. 9.6 and 9.7.

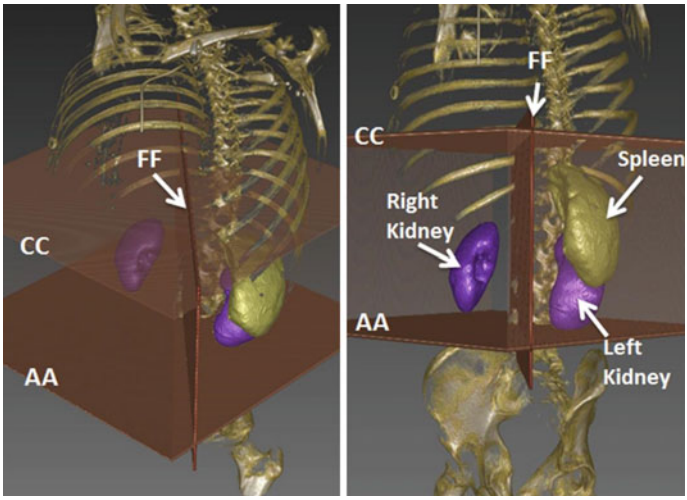

Fig. 9.6 Two views of the kidneys' and spleen's ROI. The ROI is defined by slices *AA*, *CC* and the area to the *left* of *FF* for the *left kidney* and spleen and the area to the *right* of *FF* for the *right kidney*

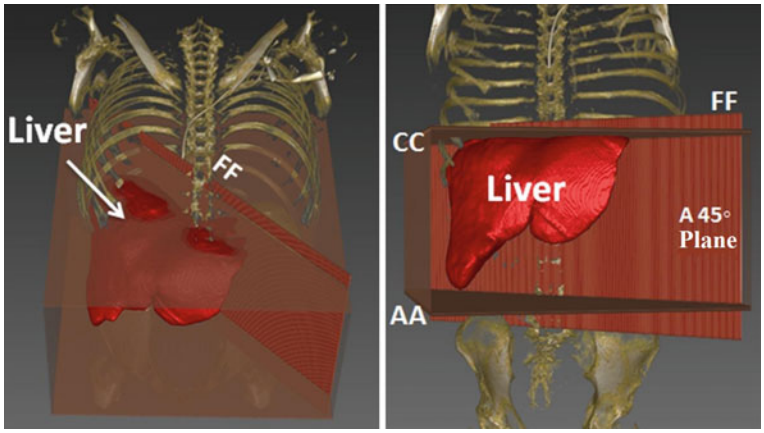

Fig. 9.7 Two views of the same liver ROI. Slices *AA*, *CC* and the area to the *right* of *FF* define the ROI

Step 2: Thresholding

We threshold the CECT scan to refine the coarse segmentation obtained from the ROI.

Lungs and Trachea: Inside the ROI, a threshold is applied to include all voxels in the range [−1000HU, −500HU], and then, the largest connected component is selected (Fig. 9.5, Step 2).

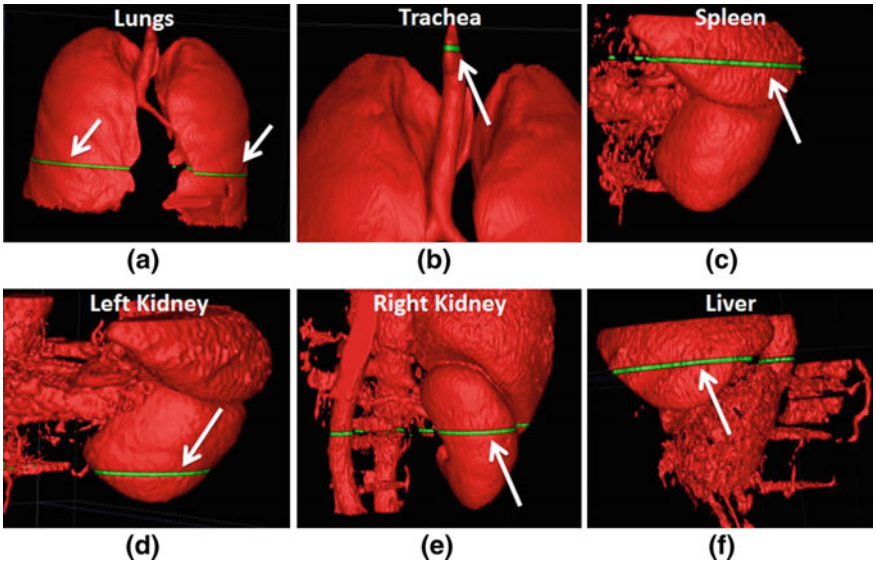

Fig. 9.8 Illustration of the location of the organs' 2D seed (*green plane*): Inside the ROI, the axial slice with the widest perimeter is selected for (a) the lungs, (d) *left kidney* and (e) the *right kidney*. The axial slice with the narrowest perimeter is selected for the trachea (b). The first slice above the *left kidney* is selected for the spleen (c) and the liver (f)

Kidney, Liver and Spleen: For the kidneys, we threshold inside the ROI by including only the voxels in the range $[\mu_{kmean},\ \mu_{BV} + 3\sigma_{BV}]$. For the liver and spleen, we only include the voxels in the range $[\mu_{BV} - 0.5\sigma_{BV},\ \mu_{kmean}]$. We use μ_{kmean} as the threshold to separate the kidneys, which are significantly richer in blood vessels, from the spleen and liver.

Step 3: 2D Seed Identification

The 2D axial slice selection is organ specific and is performed as follows:

Lungs and Trachea: Inside the lungs and trachea ROIs (Fig. 9.5, Step 1), the axial slice with the narrowest perimeter (*DD*) is selected as the 2D seed for the trachea. The axial slice with the widest perimeter (*CC*) is selected as the 2D seed for the lungs. Note that the widest axial slice of the lungs contains two connected components, for the left and right lungs (Fig. 9.8a, b).

Kidneys: Inside the kidneys' ROI, the axial slice with the widest perimeter is selected as the 2D seed for the kidneys (Fig. 9.8d, e).

Liver and Spleen: The first slice above the left kidney is selected as the 2D seed for the liver and spleen (Fig. 9.8c, f).

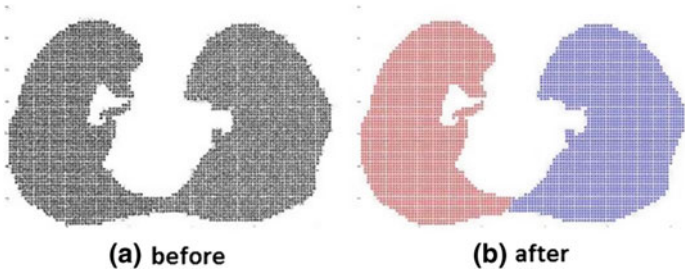

Fig. 9.9 Axial slice showing the results of the spectral cluster algorithm to isolate each lung

Step 4: Slice Region Growing

For each organ, we perform the region growing from the axial 2D seed. The seed is extended slice by slice along the axial planes, within the coarse segmentation obtained in Step 3, to include the entire organ. The unique segmentation characteristics for each organ are as follows:

Lungs: Inevitably, in the lungs, some axial slices might appear as a single connected component. To avoid this and to isolate each lung on those slices, we use the spectral clustering algorithm [20] with two clusters. Figure 9.9 illustrates the result of using the spectral clustering algorithm.

Note that the widest axial slice of the lungs, used as the 2D seeds at Step 3, occurs around the heart, which pushes the lungs out of its way, thus acting as a natural separator, so the lungs do not appear as a single connected component.

Trachea: The region growing is performed upwards to the top of the ROI and downwards to the first bifurcation.

Kidneys, Liver, Spleen: The region growing is performed upwards and downwards from the seed slice within the ROI. Between each pair of slices, the region growing continues only into the largest connected component that intersects with the current slice. All smaller intersected components are removed, as ventral cavity organs are relatively smooth, so two adjacent voxels of the same organ cannot exceed some level of variability (Fig. 9.10). This process is repeated throughout the slices inside the ROI.

9.2.4 Post-processing at the End of Process 2

A final post-processing fine-tuning sequence is performed on the kidneys, liver and spleen in order to finalize their segmentation. This post-processing sequence is different for each organ.

Kidneys: First, holes in the image are filled. Next, all connected components that have fewer than 50 pixels are removed. Then, the largest 3D connected component

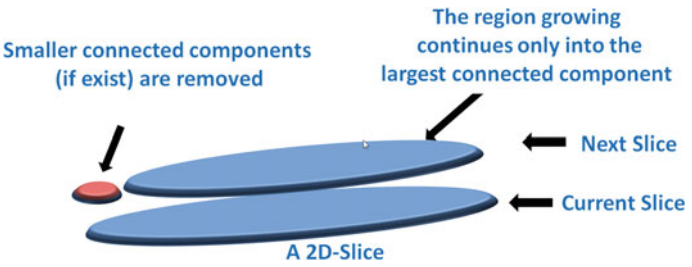

Fig. 9.10 Schematic illustration of the liver, spleen and kidneys region growing between two adjacent slices. The current slice contains a single component. The next slice contains two components. The region growing proceeds into the largest component (*blue*) that intersects with the current slice, where the smaller intersected components are removed (*red*)

is selected. And finally, a closing operation with a disc-shaped structuring element with a radius of 3 pixels is performed.

Liver: First, all connected components that have fewer than 50 pixels are removed. Next, the largest 3D-connected component is selected. And finally, holes in the image are filled.

Spleen: A closing operation with a disc-shaped structuring element with a radius of 4 pixels is performed.

Note that the morphological operators are 2D and are applied to the axial slices.

To further increase the overall accuracy and the robustness of our method, we use a simple control mechanism to detect major failures in the segmentation process. When the volume of a segmented organ is less than 30% of the mean volume for that organ from the 20 ground truths of the training set, we classified the segmentation as a failure. We exclude failure cases for two reasons. First, we follow the VISCERAL Benchmark guidelines for the results. The guidelines exclude empty files from the evaluation, so we added a quality-assurance step with a rigorous threshold to filter out these cases. Second, note that the segmentation algorithm is the first step of a content-based image retrieval (CBIR) system, the goal is to retrieve the 10–30 most relevant scans. Those failure cases are marked with N/A in Table 9.2.

9.3 The VISCERAL Benchmark

The VISCERAL Anatomy2 Benchmark dataset [17] consists of four modalities: CT and MR scans of the whole body (wb), CECT scans of the whole trunk and T1 contrast-enhanced MR scans of the abdomen. Each modality has 30 clinical scans (a training dataset of 20 scans was made available to participants before the benchmark, and a test dataset of 10 scans used only by the organizers). All scans were acquired between 2004 and 2008. Our method was submitted for the CECT whole trunk modality.

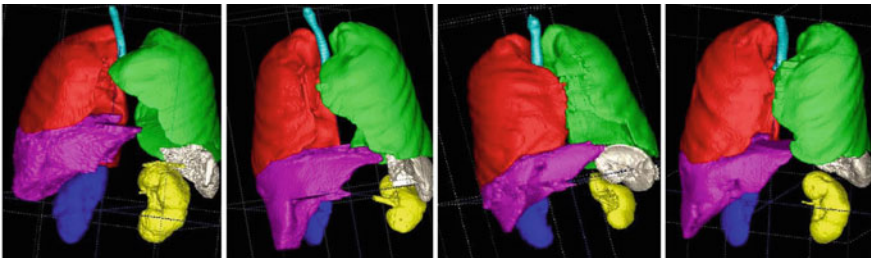

Fig. 9.11 Multiorgan segmentation results of four representative CECT scans of the VISCERAL Challenge

The CECT whole trunk scans were acquired from adult patients with malignant lymphoma. Their field of view starts between the skull base and the neck and ends at the pelvis. In-plane resolution is $0.604 - 0.793$ mm; the in-between plane resolution is 3 mm. A VISCERAL team radiologist manually produced ground truth segmentation for each scan.

The VISCERAL training and test datasets were uploaded to the Azure cloud framework. The training dataset was made available to all registered benchmark participants. In this unique cloud-based evaluation benchmark [14], the participants were required to submit their source code and the testing was conducted by the organizers. The participants received a virtual cloud computing 8-core CPU instance with 16-GB RAM. Both the executable and the required libraries were installed by the participants in the virtual machines. The test dataset was not accessible to the participants. The organizers ran the virtual machines with the participants' segmentation software on the test data. The goal of this framework is to generate an objective and unbiased evaluation of the different algorithms with the same test dataset and the same computing capabilities for all the participants.

9.4 Results and Discussion

Table 9.2 shows the results for the training dataset; Table 9.3 summarizes the results for the test dataset. The high values of DICE similarity coefficients demonstrate the reliability of our method. In the recent VISCERAL Challenge, for air-containing organs, our method was ranked as one of the top [13]. Figure 9.11 shows four representative examples of the multiorgan segmentation results.

Note that the only organ for which our segmentation averages below 90% accuracy is the liver. This stems from the fact that the liver is the most complex organ in the body, with very high variance among the individuals, and varying grey levels according to the phase in which the scan was obtained.

Our approach throughout the paper is based on the anatomical analysis. The aim of the ROIs is to identify the location of the organs defined by medical-anatomical knowledge. The thresholds for separating the kidneys from the spleen/liver are based

Table 9.2 DICE similarity score per organ for the training dataset (20 CECT scans)

Subject id	Trachea	Left lung	Right lung	Right kidney	Left kidney	Liver	Spleen
10000100	0.96	0.97	0.97	0.88	0.82	0.91	0.94
10000104	0.83	0.98	0.97	0.90	0.92	N/A	0.78
10000105	N/A	0.93	0.92	0.86	0.90	0.94	0.94
10000106	0.89	0.98	0.97	0.92	0.94	0.90	0.89
10000108	0.89	0.98	0.98	0.89	0.93	0.92	0.81
10000109	0.94	0.96	0.95	0.90	0.91	0.87	0.92
10000110	0.84	0.98	0.98	0.95	0.95	0.85	0.92
10000111	0.95	0.96	0.97	0.92	0.91	N/A	0.94
10000112	0.91	0.97	0.94	N/A	0.92	0.74	0.83
10000113	0.91	0.97	0.98	0.95	0.95	0.91	0.96
10000127	0.82	0.97	0.97	N/A	N/A	0.73	N/A
10000128	0.85	0.96	0.98	0.89	0.91	0.87	0.93
10000129	0.84	0.98	0.98	N/A	N/A	0.93	N/A
10000130	0.85	0.96	0.96	0.91	0.91	0.86	0.95
10000131	0.96	0.96	0.95	0.93	0.94	0.86	0.91
10000132	0.96	0.77	0.95	0.91	0.92	0.92	0.94
10000133	0.87	0.97	0.95	0.92	0.92	0.90	0.78
10000134	0.92	0.99	0.98	0.90	0.92	0.85	0.92
10000135	0.94	0.98	0.95	0.89	0.91	0.92	0.85
10000136	N/A	0.98	0.97	0.93	0.91	0.84	0.95
Average	**.90**	**0.96**	**0.96**	**0.91**	**0.92**	**0.87**	**0.90**

on the fact that the kidneys are significantly richer in blood vessels. The fact that the widest axial slice of the lungs occurs around the heart, which acts as a natural separator, ascertains the lungs do not appear as a single connected component at that point.

An advantage of the cloud-based evaluation framework is that it required us to develop robust and portable software, which we published as open source that can be integrated in different platforms such as the clinical environment.

If one of the organ segmentations failed during the pipeline process, all following organs will fail too. This is because of the dependency between segmentation steps. Such a scenario occurred for subjects 10000127 and 10000129 (Table 9.2), for the segmentation of the left kidney failed and as a result segmentation of all succeeding organs—spleen and the right kidney—failed. This could also happen in cases of nephrectomy (kidney removal).

Table 9.3 Results: Average DICE similarity score per organ for the test dataset (10 CECT scans)

Test dataset	Trachea	Left lung	Right lung	Right kidney	Left kidney	Spleen
	85.1	97.0	96.8	87.0	82.9	82.2

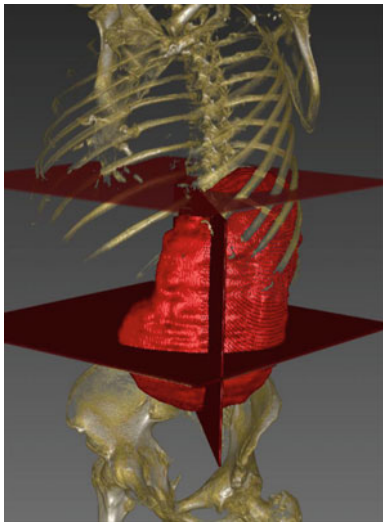

Fig. 9.12 The enlarged spleen of subject 1000112: In some rare cases, organs might extend outside the ROI; this happens in cases of enlarged organs

Note that segmentations 10000127 and 10000129 were tagged as failure by our control mechanism which excludes any segmentation result if it is below 30% of the average volume calculated for the organ. Working in the field of big data, we consider it much more preferable to retrieve fewer cases, but be more assured they are highly relevant cases, than to risk retrieving less relevant cases, because they were mis-segmented.

Another limitation can come from the construction of the ROI. There are some rare cases where the organs extend outside the ROI; this happens in cases of enlarged organs that vary from the standard shape. Such an example is shown in Fig. 9.12.

9.5 VISCERAL Benchmark Perspective

Five other groups participated in the VISCERAL Anatomy2 Benchmark for the CECT modality. Below is a short description of their methods, followed by a short discussion.

Kechichian et al. [15] propose a generic method based on a multilabel graph cut optimization approach that uses location likelihood of organs and prior information of spatial relationships between them. Organ atlases are mapped and used. To derive organ intensity likelihoods, prior and likelihood models are then introduced in a joint centroidal Voronoi image clustering and graph cut multiobject segmentation framework. Wang et al. [32] segmented 10 anatomical structures in CT contrast-enhanced and non-enhanced scans. Their multiorgan segmentation pipeline follows a top-down approach based on the level set segmentation of the ventral cavity. After dividing the cavity into the thoracic and abdominal cavities, the major structures are

segmented based on statistical shape and their location information is used to segment the lower-level structures. Jimenez del Toro et al. [12] segment structures in CT contrast-enhanced and non-enhanced scans with a hierarchical multiatlas approach. Based on the spatial anatomical correlations between the organs, the bigger and higher-contrast organs are segmented first. These initial volume transformations form the basis for identifying the smaller structures with less defined boundaries. Goksel et al. [7] describe segmentation methods for both CT and MR anatomical structures. They use a multiatlas-based technique that uses Markov random fields to guide the registrations. A multiatlas template-based approach fuses the different deformable registrations to detect the segmentation. Xuhui et al. [34] propose a coarse liver segmentation using prior models for the shape, appearance and contextual information of the liver. An AdaBoost voxel-based classifier creates a liver probability map that is augmented in the last step with freeform deformation with a gradient appearance model. Next, we describe and compare these methods according to the different characteristics.

The methods of [7, 12, 15] are based on the registration to an atlas while the methods of [32, 34] require registration to a statistical shape model. Registration requires a presegmented dataset and is a time-consuming process and subject to inaccuracies. Only our work obviates the need for costly registration.

Most of the methods, including [12, 15, 32, 34] and our method, are based on a hierarchical process—organs are segmented in a predefined order to minimize segmentation errors and that of [7] segments all organs at once by image registration to a multiorgan atlas. We believe that hierarchical-based methods yield better results when compared to the method of [7] because they allow mutual information sharing between the segmentation processes of different organs.

While the VISCERAL Challenge is aimed at both enhanced and non-enhanced CT scans, our method is currently applicable only for enhanced CTs. Other methods are also applicable for non-enhanced CTs, thanks to the use of atlas/shape information. Currently, we are working on adapting our approach for non-enhanced CTs as well.

9.6 Conclusion

We have presented a new fully automatic atlas-free segmentation method of multiple organs of the ventral cavity in CT scans. Our method is unique in that it obviates the need for a predefined atlas and/or costly registration and in that it uses the same generic segmentation approach for all organs. Experimental results on 20 CECT scans of the VISCERAL Anatomy2 training dataset and 10 CECT scans of the Anatomy2 test dataset yield an average DICE volume overlap similarity score of 90.95 and 88.50%, respectively.

Automatic segmentation of anatomical structures in CT scans is an essential step in the analysis of radiological patient data and is a prerequisite for large-scale content-based image retrieval (CBIR) systems. Worldwide, the number of volumetric medical images (CT, MRI, etc.) reaches into the hundreds of millions per year and represents

the largest single component of the medical health record. This untapped gold mine of medical data awaits the application of big data analytics, such as CBIR, to enable large-scale population and epidemiological studies, preventive medicine by early detection and assist radiologists in the decision-making process. The cloud-based evaluation framework of the VISCERAL Benchmarks [14] required source code to be submitted for testing by the organizers, the code was independently tested and we published it online[2]—it is now freely available for the benefit of the CBIR community. Future work consists of extending our approach to additional imaging modalities such as non-enhanced CT, handling scans of patients with organs missing, and testing the applicability of our method in an end-to-end CBIR scheme.

References

1. Aljabar P, Heckemann RA, Hammers A, Hajnal JV, Rueckert D (2009) Multi-atlas based segmentation of brain images: atlas selection and its effect on accuracy. NeuroImage 46(3):726–738
2. Boykov Y, Funka-Lea G (2006) Graph cuts and efficient N-D image segmentation. Int J Comput Vis 70(2):109–131
3. Caselles V, Kimmel R, Sapiro G (1997) Geodesic active contours. Int J Comput Vis 22(1):61–79
4. Deserno TM, Antani S, Long R (2009) Ontology of gaps in content-based image retrieval. J Digit Imaging 22(2):202–215
5. Freiman M, Eliassaf O, Taieb Y, Joskowicz L, Azraq Y, Sosna J (2008) An iterative bayesian approach for nearly automatic liver segmentation: algorithm and validation. Int J Comput Assist Radiol Surg 3(5):439–446
6. Freiman M, Kronman A, Esses SJ, Joskowicz L, Sosna J (2010) Non-parametric iterative model constraint graph min-cut for automatic kidney segmentation. Med Image Comput Comput Assist Interv, 13:73–80
7. Goksel O, Gass T, Szekely G (2014) Segmentation and landmark localization based on multiple atlases. In: CEUR workshop proceedings, pp 37–43
8. Gudewar AD, Ragha LR (2012) Ontology to improve CBIR system. Int J Comput Appl 52(21):23–30
9. Haris K, Efstratiadis SN, Maglaveras N, Katsaggelos AK (1998) Hybrid image segmentation using watershed and fast region merging. IEEE Trans Image Process 7(12):1684–1699
10. Heimann T, Meinzer HP (2009) Statistical shape models for 3D medical image segmentation: a review. Med Image Anal 13(4):543–563
11. Hwang KH, Lee H, Choi D (2012) Medical image retrieval: past and present. Healthc Inf Res 18(1):3–9
12. Jiménez del Toro ÓA, Müller H (2014) Multi-structure atlas-based segmentation using anatomical regions of interest. In: Menze B, Langs G, Montillo A, Kelm M, Müller H, Tu Z (eds) MCV 2013. LNCS, vol 8331. Springer, Cham, pp 217–221. doi:10.1007/978-3-319-05530-5_21
13. Jiménez del Toro OA, Goksel O, Menze B, Müller H, Langs G, Weber MA, Eggel I, Gruenberg K, Holzer M, Jakab A, Kotsios-Kontokotsios G, Krenn M, Fernandez TS, Schaer R, Taha AA, Winterstein M, Hanbury A (2014) VISCERAL—VISual concept extraction challenge in RAdioLogy: ISBI 2014 challenge organization. In: Goksel O (ed) Proceedings of the VISCERAL challenge at ISBI, Beijing, China, no. 1194 in CEUR workshop proceedings, pp 6–15. http://ceur-ws.org/Vol-1194/visceralISBI14-0.pdf

[2] http://www.cs.huji.ac.il/~caslab.

14. Jiménez del Toro OA, Müller H, Krenn M, Gruenberg K, Taha AA, Winterstein M, Eggel I, Foncubierta-Rodriguez A, Goksel O, Jakab A, Kontokotsios G, Langs G, Menze B, Fernandez TS, Schaer R, Walleyo A, Weber MA, Cid YD, Gass T, Heinrich M, Jia F, Kahl F, Kechichian R, Mai D, Spanier A, Vincent G, Wang C, Wyeth D, Hanbury A (2016) Cloud-based evaluation of anatomical structure segmentation and landmark detection algorithms: visceral anatomy benchmarks. IEEE Trans Med Imaging 99:1–1. doi:10.1109/TMI.2016.2578680
15. Kéchichian R, Valette S, Sdika M, Desvignes M (2014) Automatic 3D multiorgan segmentation via clustering and graph cut using spatial relations and hierarchically-registered atlases. In: Menze B, Langs G, Montillo A, Kelm M, Müller H, Zhang S, Cai WT, Metaxas D (eds) MCV 2014. LNCS, vol 8848. Springer, Cham, pp 201–209. doi:10.1007/978-3-319-13972-2_19
16. Kronman A, Joskowicz L, Sosna J (2012) Anatomical structures segmentation by spherical 3D ray casting and gradient domain editing. In: Ayache N, Delingette H, Golland P, Mori K (eds) MICCAI 2012. LNCS, vol 7511. Springer, Heidelberg, pp 363–370. doi:10.1007/978-3-642-33418-4_45
17. Langs G, Hanbury A, Menze B, Müller H (2013) VISCERAL: towards large data in medical imaging — challenges and directions. In: Greenspan H, Müller H, Syeda-Mahmood T (eds) MCBR-CDS 2012. LNCS, vol 7723. Springer, Heidelberg, pp 92–98. doi:10.1007/978-3-642-36678-9_9
18. Mharib AM, Rahman A, Mashohor S, Binti R (2012) Survey on liver CT image segmentation methods. Artif Intell Rev 37(2):83–95
19. Müller H, Zhou X, Depeursinge A, Pitkanen M, Iavindrasana J, Geissbuhler A (2007) Medical visual information retrieval: state of the art and challenges ahead. In: IEEE international conference on multimedia and expo. IEEE, pp 683–686
20. Ng AY, Jordan MI, Weiss Y (2002) On spectral clustering: analysis and an algorithm. Adv Neural Inf Process Syst 2:849–856
21. Okada T, Yokota K, Hori M, Nakamoto M, Nakamura H, Sato Y (2008) Construction of hierarchical multi-organ statistical atlases and their application to multi-organ segmentation from CT images. In: Metaxas D, Axel L, Fichtinger G, Székely G (eds) MICCAI 2008. LNCS, vol 5241. Springer, Heidelberg, pp 502–509. doi:10.1007/978-3-540-85988-8_60
22. Pham DL, Xu C, Prince JL (2000) Current methods in medical image segmentation. Annu Rev Biomed Eng 2(1):315–337
23. Rohlfing T, Brandt R, Menzel R, Russakoff DB, Maurer CR (2005) Quo vadis, atlas-based segmentation? Springer, Boston
24. Rubin DL (2011) Informatics in radiology: measuring and improving quality in radiology: meeting the challenge with informatics. Radiographics 31(6):1511–1527
25. Rubin DL (2012) Finding the meaning in images: annotation and image markup (maintained). Philos Psychiatry Psychol 18(4):311–318
26. Schmidt G, Athelogou M (2007) Cognition network technology for a fully automated 3D segmentation of liver. In: Proceedings of the MICCAI workshop 3-D segmentation clinic: a grand, challenge, pp 125–133
27. Simonyan K, Zisserman A, Criminisi A (2011) Immediate structured visual search for medical images. In: Fichtinger G, Martel A, Peters T (eds) MICCAI 2011. LNCS, vol 6893. Springer, Heidelberg, pp 288–296. doi:10.1007/978-3-642-23626-6_36
28. Sluimer I, Schilham A, Prokop M, van Ginneken B (2006) Computer analysis of computed tomography scans of the lung: a survey. IEEE Trans Med Imaging 25:385–405
29. Tong T, Wolz R, Wang Z, Gao Q, Misawa K, Fujiwara M, Mori K, Hajnal JV, Rueckert D (2015) Discriminative dictionary learning for abdominal multi-organ segmentation. Med Image Anal 23(1):92–104
30. Tsai A, Yezzi A Jr, Wells W, Tempany C, Tucker D, Fan A, Grimson WE, Willsky A (2003) A shape-based approach to the segmentation of medical imagery using level sets. Med Imaging 22(2):137–154
31. Valente F, Costa C, Silva A (2013) Content based retrieval systems in a clinical context, chap 1. In: Felix Erondu O (ed) Medical imaging in clinical practice. InTech, Rijeka

32. Wang C, Smedby O (2014) Automatic multi-organ segmentation in non-enhanced CT datasets using hierarchical shape priors. In: 22nd international conference on pattern recognition (ICPR), pp 3327–3332
33. Wolz R, Chu C, Misawa K, Mori K, Rueckert D (2012) Multi-organ abdominal CT segmentation using hierarchically weighted subject-specific atlases. In: Ayache N, Delingette H, Golland P, Mori K (eds) MICCAI 2012. LNCS, vol 7510. Springer, Heidelberg, pp 10–17. doi:10.1007/978-3-642-33415-3_2
34. Li X, Huang C, Jia F, Li Z, Fang C, Fan Y (2014) Automatic liver segmentation using statistical prior models and free-form deformation. In: Menze B, Langs G, Montillo A, Kelm M, Müller H, Zhang S, Cai WT, Metaxas D (eds) MCV 2014. LNCS, vol 8848. Springer, Cham, pp 181–188. doi:10.1007/978-3-319-13972-2_17